Measuring the Magnetic Polarizability Tensor Using an Axial Multi-Coil Geometry

Toykan Özdeğer, John L. Davidson, Wouter van Verre, Liam A. Marsh, *Member, IEEE*, William R. B. Lionheart, and Anthony J. Peyton

***Abstract*—The Magnetic Polarizability Tensor (MPT) is a representative property of an electrically conducting or magnetic object that includes information about the object's characteristics such as, shape, size and material. The MPT is especially relevant to metal detection (MD) and can be used to improve MD performance by helping to distinguish between objects. This paper describes an instrument intended to measure the MPT of objects such as anti-personnel landmines and metallic clutter, up to 130 mm in diameter. The instrument uses a novel multi-coil geometry to generate a uniform electromagnetic field over the volume containing the test object to accurately determine the MPT. Performance tests of the system shows peak variance in the MPT is approximately 15 mm^3. Typical experimental repeatability is better than one percent for tests involving copper disks. Additionally, simulated data as well as previously published simulated and experimental data are used as a validation method of the experimental results. Good agreement between these and the measured MPTs of example targets are seen, proving the system's capability of characterizing metallic objects.**

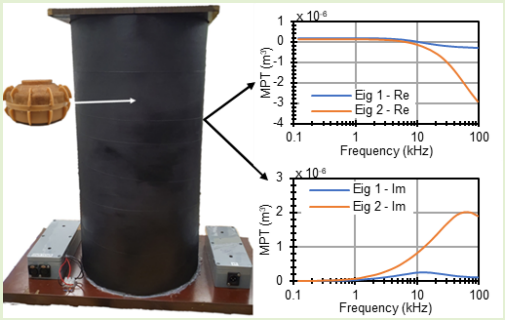

***Index Terms*— Electromagnetic Induction Spectroscopy, Magnetic Polarizability Tensor, metal detection, metal classification.**

I. Introduction

ANTI-PERSONNEL (AP) landmines continue to be a significant problem in post-conflict areas as they can remain armed long after the conflict has ended. Clearing an area of landmines is a slow and expensive process and so landmines may remain undisturbed for many years. This renders large areas of land unusable, preventing people from using this land for agriculture, social and economic activity, or housing. However, the biggest problem is that a landmine is victim activated and cannot distinguish between military personnel or civilians. Therefore, landmines in post-conflict areas mostly cause damage to non-military people [1], [2]. It is estimated that there are tens of millions of buried AP landmines worldwide, which means with the current rate of demining, it will take many years to clear all post-conflict areas of landmines [3], [4].

Metal detection (MD) has been the common way to detect landmines in humanitarian demining, which has more recently been augmented by ground penetrating radar (GPR). However, land in post-conflict areas usually have a high density of metallic clutter in the soil, which results in a high false alarm rate (FAR) from MD, which can hamper the demining process. In some fields, deminers can find 100 clutter objects for each landmine [5]. Clearly better differentiation would help.

The Magnetic Polarizability Tensor (MPT) is a representative electromagnetic object property, which depends on the size, material and shape of an object. Recent progress in mathematical theory has demonstrated that the MPT is the coefficient array in the first term in an asymptotic expansion of the perturbed field [6]–[9]. Although the motivation of this paper is toward humanitarian demining, the MPT and Electromagnetic Induction Spectroscopy have also been successfully applied widely in MD, for example to the detection of unexploded ordnance [10]–[12], walk-through metal detectors [13], metal recycling [14], workpiece recognition [15], non-destructive testing [16]–[18] and buried object detection [19]. MPT and broadband inductive sensing have also been previously proposed for landmine detection [20]–[25].

Manuscript received May 10, 2021; accepted May 28, 2021. Date of publication June 14, 2021; date of current version August 31, 2021. This work was supported in part by the Engineering and Physical Sciences Research Council under Grant EP/R002177 and in part by the Sir Bobby Charlton Foundation. The associate editor coordinating the review of this article and approving it for publication was Dr. Jürgen Kosel. *(Corresponding author: Toykan Özdeğer.)*

Toykan Özdeğer, John L. Davidson, Wouter van Verre, Liam A. Marsh, and Anthony J. Peyton are with the Department of Electrical and Electronics Engineering, The University of Manchester, Manchester M13 9PL, U.K. (e-mail: toykan.ozdeger@manchester.ac.uk; j.davidson-2@manchester.ac.uk; wouter.vanverre@manchester.ac.uk; liam.marsh@manchester.ac.uk; a.peyton@manchester.ac.uk).

William R. B. Lionheart is with the Department of Mathematics, The University of Manchester, Manchester M13 9PL, U.K. (e-mail: bill.lionheart@manchester.ac.uk).

Digital Object Identifier 10.1109/JSEN.2021.3088809

If an MPT library of landmines and common metallic clutter found in post-conflict areas are to be constructed, landmine detectors could utilize this library to reduce FAR and speed up the demining process, especially when coupled to secondary detection such as GPR.

Small-scale multiple coil arrangements have been reported in the area of induction spectrometry. For example, Goldfarb and Minervini [26] reported on the theory of mutual inductance applied to AC spectrometry for small cylindrical specimens. Additionally, West and Bailey [27] describe a simplistic six coil arrangement used for the measurement of the complex magnetic susceptibility of soils. However, those systems have not been used to produce absolute measurements of the MPT nor are of sufficient size to enable measurements to be taken on larger objects such as AP landmines.

Previously, Scott and Larson have established an experimental test facility [24], [25] which enables the measurement of the electromagnetic induction (EMI) response of target objects as a function of location and orientation. The facility includes a cart-based broadband EMI data collection system [28] and a laboratory-based positioner [29] with 3D automated translational and semi-automated rotational stages. Additionally, Scott and Larson developed dipole expansion and inversion techniques used to measure the magnetic susceptibility of soils and the polarizability of metallic objects [25], [30]. Reported targets have included coplanar metal loops, AP landmines and clutter items such as rifle cartridges and steel nails. Good agreement between measured and theoretical model parameters are presented for the case of single and triple conducting loop targets as a function of relaxation frequency.

At the University of Manchester, an MPT measurement system was previously built in [31], which was reported to characterize MPTs of AP landmine surrogates and small metal objects such as common clutter items found in post-conflict areas [32]. However, measurements from the coil arrangement were prone to drift, the system did not have a large region of uniform electromagnetic field for measuring larger AP landmines and was unable to characterize large objects due to the small size of the measurement space. Additionally, the previous system only utilized a simple target manipulator, which was unable to provide precise orientation of large targets.

This paper describes a new multi-coil arrangement with custom electronics system and software, which is better suited to the characterization of large objects such as landmines and landmine surrogates. A wider frequency spectrum was also used in the new system, extending to a lower frequency of 100 Hz, thereby improving the characterization of objects of lower conductivity and higher permeability. Commercial demining metal detectors do not presently provide direct MPT measurements. Additionally, although some experimental and laboratory-based systems [10]–[12], [28]–[30] have generated MPTs, these have often been for either large UXO type targets or for test objects which are difficult to replicate accurately in terms of size, shape, and material composition. Therefore, to assess the performance of the new system, we have compared the MPT data with previously obtained and published US coins MPT data from [33] and AP landmine MPT data from [32].

In this paper we start in Section II with describing the MPT, how it can be measured experimentally and the design of a coil arrangement for this purpose. Section III gives details of the experimental setup for the MPT measurement arrangement including the system electronics, controlling software for data acquisition and the target orientation manipulator. Section IV describes the methods used for characterization of the coils, assessment of overall system performance, setup calibration and acquisition of target data. Section V describes Finite Element Method (FEM) simulations of the coil arrangement and a sub-set of target objects. Section VI discusses the results of the coil characterization and system performance tests. The paper then shows the experimental results from the system and compares them with previously published measured and simulated data in section VII. Section VIII concludes the paper with a discussion of system potential and further work.

II. Background

A. Magnetic Polarizability Tensor

Every conductive object gives a response to an applied electromagnetic field. In the eddy current approximation, the leading order term of the response is determined by the MPT of the object [34]. The MPT is an object specific property that depends on the shape, size, object's orientation and material composition. Consequently, when a metal detector generates an electromagnetic field near an object, the response that is measured by the receive coil is determined to a first approximation by the MPT [31]–[37]. The MPT in (1) is a 3×3 matrix of complex, frequency dependent coefficients. At a fixed frequency f, low enough for the eddy current approximation to be valid, the MPT matrix is symmetric and has six unique complex coefficients.

$$\boldsymbol{M}(f)=\begin{bmatrix} M'_{xx}+jM_{xx}'' & M'_{xy}+jM_{xy}'' & M'_{xz}+jM_{xz}'' \\ M'_{yx}+jM_{yx}'' & M'_{yy}+jM_{yy}'' & M'_{yz}+jM_{yz}'' \\ M'_{zx}+jM_{zx}'' & M'_{zy}+jM_{zy}'' & M'_{zz}+jM_{zz}'' \end{bmatrix} \quad (1)$$

If constructing the MPT matrix by measurements, at least six complex suitably chosen measurements of the object are needed. However, in practice more orientations are used to improve accuracy [32]. The induced voltage V_{ind} in a receive coil, where I is the virtual electrical current in the receive coil satisfies (2). $\boldsymbol{H}$ is the primary electromagnetic field as a vector representing the produced field by the coil in three-dimensional space, superscript T means transposed and subscript T and R correspond to transmit and receive coils, respectively.

$$V_{ind} \cong -j2\pi f \frac{\mu_0}{I} \boldsymbol{H_T^T M H_R} \quad (2)$$

To get coefficients in $\boldsymbol{M}$, multiple independent complex measurements of V_{ind} at each frequency are required for different transmitter and receiver field orientations to build a system of linear equations. To calculate all six unique components in the MPT matrix, the object should be rotated into at least six different orientations. By measuring V_{ind} and calculating alignment of $\boldsymbol{H_T}$ and $\boldsymbol{H_R}$ with the target, a linear equation for each orientation can be constructed using (2), where the only unknown is $\boldsymbol{M}$. Then, least squares method

can be used to calculate the MPT coefficients [38]. A nearly uniform electromagnetic field is needed near the object for this application as when non-uniform field is used, higher order terms in the asymptotic expansion also become apparent [9]. For calculating rotated electromagnetic fields of transmit and receive coils for each orientation, which are same for both coils if they are coaxial, rotation matrix can be used as in (3):

$$\boldsymbol{H^1 = R\ H^0} \tag{3}$$

The MPT is frequency dependent, which means that measuring MPT at different frequencies provides a more detailed information set so a stronger basis for discrimination. However, the orientation dependency of the MPT makes it difficult to characterize a target object, where the orientation is unknown. Therefore, eigenvalues of the MPTs are used in classification, which are not orientation dependent. Eigenvalues of MPT are responses generated when the primary field is aligned with one of object's principal axes [39]. Diagonal matrix, $\boldsymbol{\Lambda}$, in (4) shows eigenvalues of the MPT matrix $\boldsymbol{M}$.

$$\boldsymbol{\Lambda}(f) = \begin{bmatrix} \boldsymbol{\Lambda}_{xx}{}' + j\boldsymbol{\Lambda}_{xx}{}'' & 0 & 0 \\ 0 & \boldsymbol{\Lambda}_{yy}{}' + j\boldsymbol{\Lambda}_{yy}{}'' & 0 \\ 0 & 0 & \boldsymbol{\Lambda}_{zz}{}' + j\boldsymbol{\Lambda}_{zz}{}'' \end{bmatrix} \tag{4}$$

B. Coil Design

To calculate the MPT of an object, the applied field needs to be accurately known. One of the key requirements of the system is to generate a parallel uniform magnetic field over a region of approximately 13 cm × 13 cm × 13 cm. This volume space being representative of a typical AP landmine or landmine surrogate [40]. To achieve uniformity over this volume the coil arrangement design is based on Helmholtz coil [41] principles and the application of the Biot-Savart Law.

According to Biot-Savart Law in (5), a magnetic field $\vec{\boldsymbol{B}}$ is produced when a current I passes through a conductor with linear segment $\boldsymbol{D\vec{L}}$, where $\vec{\boldsymbol{r}}^2$ is the displacement vector between point of observation and midpoint $\hat{\boldsymbol{r}}$:

$$\vec{\boldsymbol{B}} = \frac{\mu_0 I}{4\pi} \oint \frac{\boldsymbol{D\vec{L}} \times \hat{\boldsymbol{r}}}{\vec{\boldsymbol{r}}^2} \tag{5}$$

Circular coils could be represented by piecewise linear elements. The magnetic field generated by each coil segment can then be calculated using (5).

Individual coil arrangements of candidate systems were generated using bespoke MATLAB based code to calculate the field over the desired volume. Coil geometry variables included the number of coils, the coil positions and the number of turns. A bespoke optimizer algorithm utilizing the Biot-Savart Law and Helmholtz coil principles determined field distributions. The optimizer algorithm generated multiple geometries that could create a uniform field. One of the generated geometries from the optimizer was chosen that best satisfied the most appropriate practical coil arrangement.

III. Experimental Setup

A. System Overview

The main system consists of three main parts, which are a coaxial coil arrangement, system electronics and control software on a PC. The custom-made control software is used to transmit control signals e.g. frequency, amplitude and digital signal processing settings to a microcontroller. The microcontroller is then used to generate excitation signals for the power amplifiers driving the transmit coils. Measurement signals from the receive coils are filtered and amplified by bespoke receive electronics. These measurements are converted to transimpedance values by the microcontroller after applying digital signal processing (DSP) and sent to the PC. Value averaging and MPT inversion are then performed by the control software. The system schematic is shown in Fig. 1.

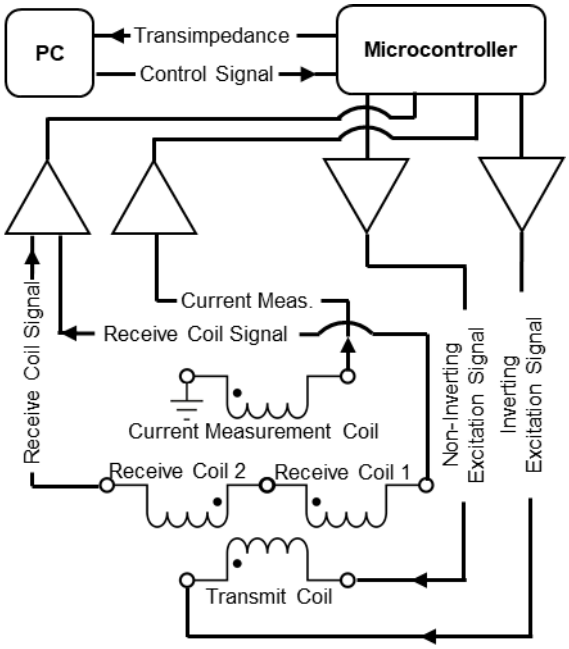

Fig. 1. System schematic showing signal routing between coils, electronics and the data acquisition PC.

B. Coil Arrangement

The coil arrangement in Fig. 2 consists of a coaxial transmit coil with 240 mm diameter and two coaxial receive coils with 220 mm diameter. Additionally, a two-turn pick-up coil positioned at the base of the coils is used for current measurement. Position of the pick-up was deemed to give minimal interaction with target objects. Design of the coils are based on the method described in section II-B and the overall height of the resulting coil arrangement is 500 mm. The transmit coil is made up of 2.1 mm enamelled copper wire wound as nine separate coil sections (turns: 11:3:5:5:5:5:5:3:11) connected in series addition. The two receive coils are connected in series opposition with each coil made up of 1.2 mm PVC insulated wire wound as four coil sections (turn: 27:18:18:49:49:18:18:27). The coils are optimized for the range between 100 Hz to 100 kHz so the resonant frequencies of the transmit and receive coil impedances are outside of the operating frequency spectrum. All coils are wound around glass fibre reinforced plastic hollow cylinders and are encapsulated in epoxy resin. The arrangement is painted with conductive

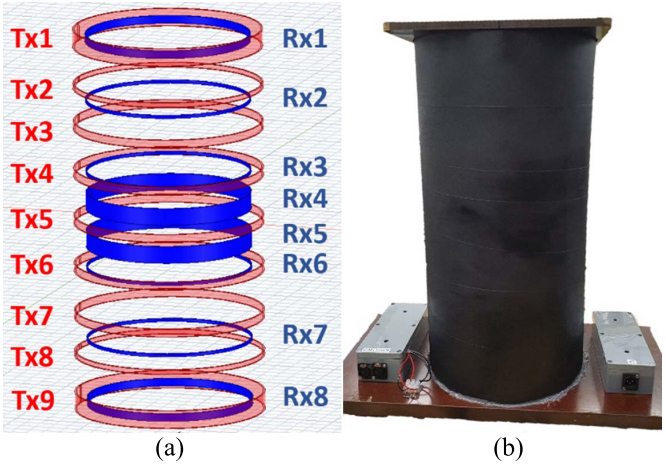

Fig. 2. The coil arrangement. Figure (a) is the schematic of the coil geometry and (b) the constructed coil arrangement.

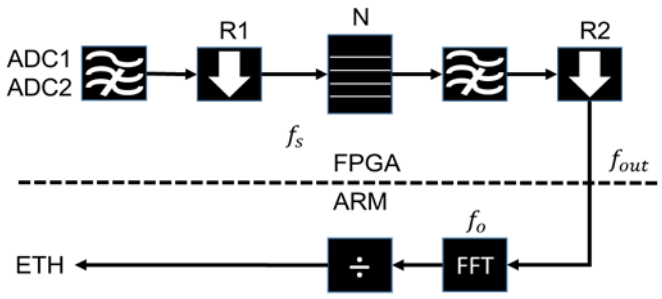

Fig. 3. Input data signal processing chain.

paint (surface resistivity: 55Ω/sq/50 microns) for electrostatic shielding.

C. Electronics

Main system electronics consists of transmit and receive electronics, power supply units and the microcontroller. The system is powered by two 18 V, 350 W power supply units (PSU) for the amplifiers and a 12 V, 80 W PSU for the microcontroller and electronics box cooling fans. A Red Pitaya model (STEMlab 125-14) is used as controller and signal processor for the system. The transmit electronics are implemented on a four-layer PCB and consists of an instrumentation amplifier, twenty power amplifiers and a band pass filter at the input for removing both AC and Digital-to-Analogue Converter's (DAC) switching noise. Half of the power amplifiers are configured as non-inverting while the rest are configured as inverting amplifiers. Each amplifier (Analog Devices LT 1210) is powered with ±18 V and can output 32 V peak-to-peak voltage. By utilizing ten inverting and ten non-inverting configurations working in parallel in a differential configuration, the transmit circuit is able to output 64 V peak-to-peak at 10 A (640 W reactive power) to the transmit coil. Receive electronics consists of two identical circuits on two-layer PCBs, each consisting of an instrumentation amplifier (Analog Devices AD8429) and an active band-pass filter.

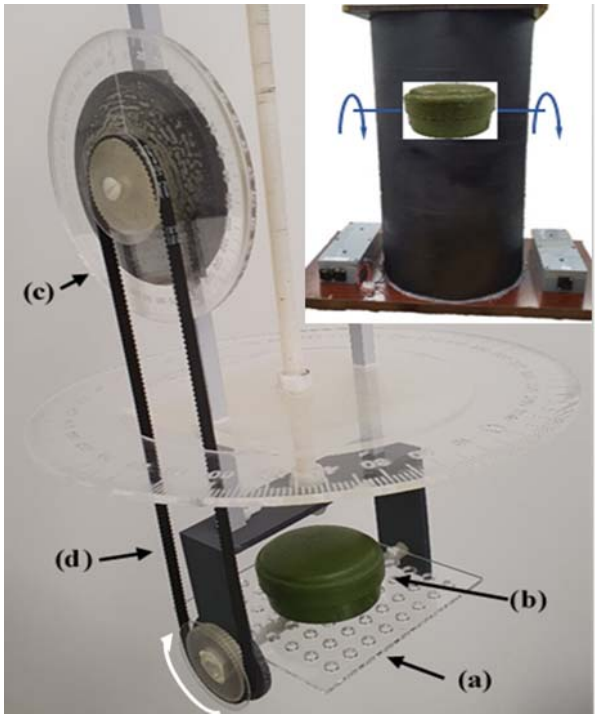

Fig. 4. Mechanical orientation manipulator 3D model showing (a) the target rotating plate, (b) Type 72A landmine surrogate, (c) measurement protractor and (d) the manually operated drive belt.

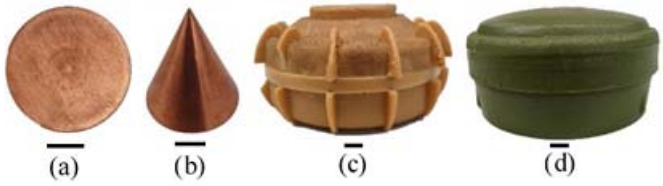

Fig. 5. Example target test objects showing copper disk, cone and AP landmine surrogates. Object (a) copper disk viewed from above and measuring 30 mm in diameter and 2 mm in thickness, (b) copper cone measuring 30 mm in height with a 30 mm diameter base, (c) TS-50 landmine surrogate and (d) Type 72A landmine surrogate. Black lines under each object represent a centimeter for scale.

D. Data Acquisition and Digital Signal Processing

The data acquisition and processing are performed by a Xilinx Zynq7000 system-on-chip (SoC), combining a dual-core ARM Cortex A7 processing and Xilinx 7-series FPGA. The SoC is mounted on a Red Pitaya, which also includes two 125 MSPS, 14-bit, Analogue-to-Digital Converter (ADC) channels and two DAC channels, also at 125 MSPS and 14-bits. The ADCs and DACs are interfaced with the FPGA fabric in the SoC, to ensure accurate timing between all four channels. The system is modified from one previously designed spectroscopic metal detector [42], [43]. The data processing on the SoC is split between the FPGA fabric and the ARM cores; the full processing chain is shown in Fig. 3 in block form.

The first step is a down sampling low-pass filter (with rate *R1*), followed by a step, which generates blocks with N samples. These blocks are then further down sampled (by a

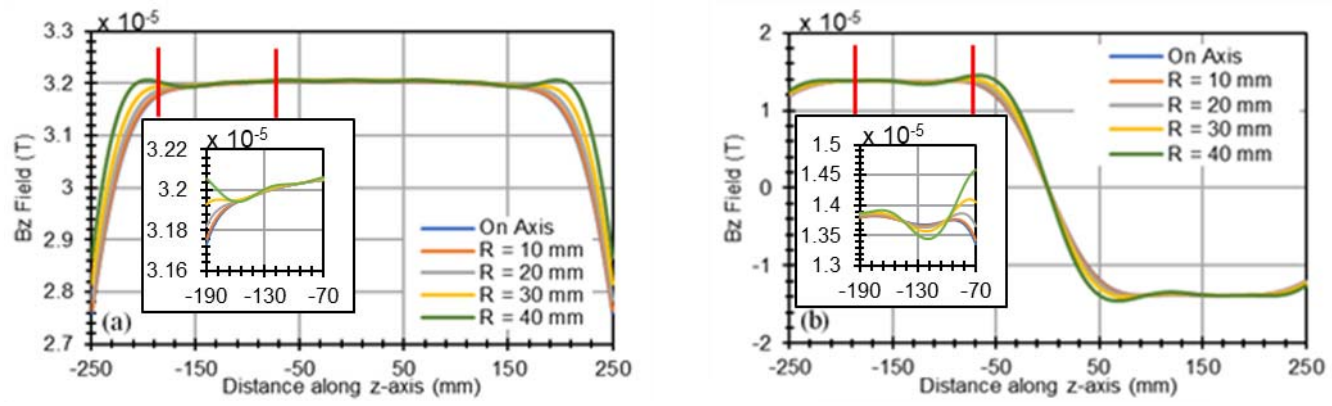

Fig. 6. Simulations of the magnetic field inside the coil system for the non-target case when transmit and receive coils are individually driven by an electric current; (a) transmit coil and (b) receive coil excitation. The measurement region is between the red vertical lines shown in the figure. The subplots within the figure show the field data within the measurement region at an enhanced scale.

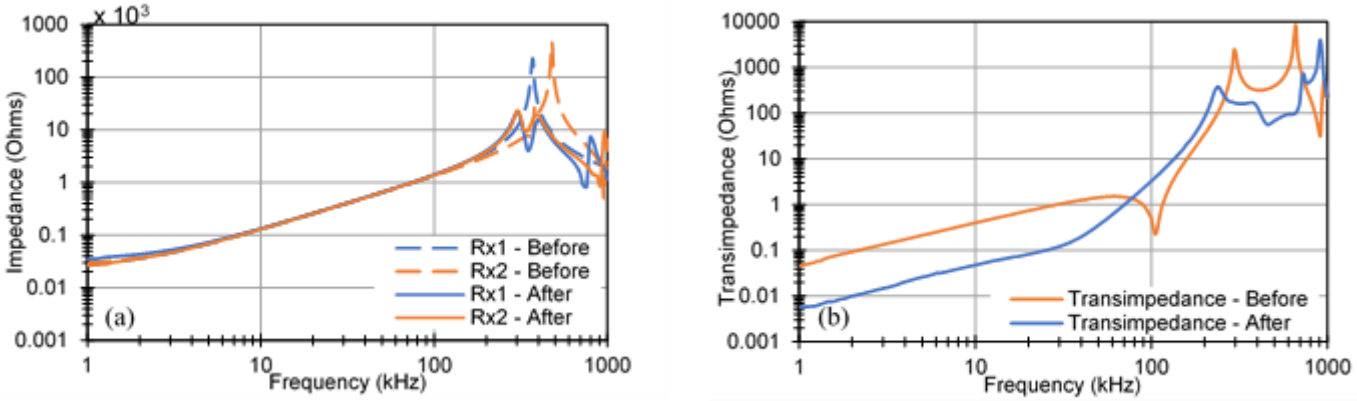

Fig. 7. (a) shows individual impedance curves of the receive coils before and after balancing the impedances while (b) shows the transimpedance between transmit coil and the receive coils, connected in series opposition, before and after the receive coils were balanced.

rate *R2*) and sent to the ARM cores. The samples are then transformed using an N-point RFFT and the harmonics of interest are extracted. The final output is calculated by dividing the extracted harmonics from *ADC1* by *ADC2*, to calculate the transimpedance. The results are transmitted to the host PC via Ethernet, using Linux on the ARM processor. The effective sampling frequency, output data rate and the fundamental frequency of the system are given in (6), (7) and (8) respectively, where ADC frequency (f_{ADC}) is always 125 MSPS.

$$f_s = \frac{f_{ADC}}{R1} \tag{6}$$

$$f_{out} = \frac{f_s}{N \times R2} \tag{7}$$

$$f_0 = \frac{f_s}{N} \tag{8}$$

The output signal path consists of a lookup table in the FPGA (of length N) for the transmit signal, which is read at the sampling frequency f_s. The data can be output at this rate, or up sampled to f_{ADC} via a linear interpolator or cascaded integrator-comb filter, which can be configured at runtime. The parameters *R1*, *R2* and N are also configurable at runtime, so that the sampling frequency, fundamental frequency and output frequencies can be configured depending on the application needs. A low fundamental frequency reduces the acquisition speed of the system. Therefore, in this experiment the parameters *R1* and N were changed as the frequency sweep progresses. This allows for granular sweep at low frequencies, while speeding up the acquisition rate at higher frequencies.

E. Control Software

The control software was written in Python 3.7 and allows the user to set experiment settings by a graphical user interface (GUI). The control of frequency sweeps, data logging and processing, MPT inversion and plotting are done automatically by the control software. The final output folder contains raw data, calibrated transimpedance values and MPT eigenvalues.

F. Target Orientation Manipulator

The custom-built target orientation manipulator shown in Fig. 4 is used to place and rotate objects in the coil arrangement, which has rotational precision of approximately 1°. It is manually operated and can rotate target objects around one axis. This means that only objects with symmetrical geometry can be measured as this methodology assumes the axis of rotation is aligned with an eigenvector of the object.

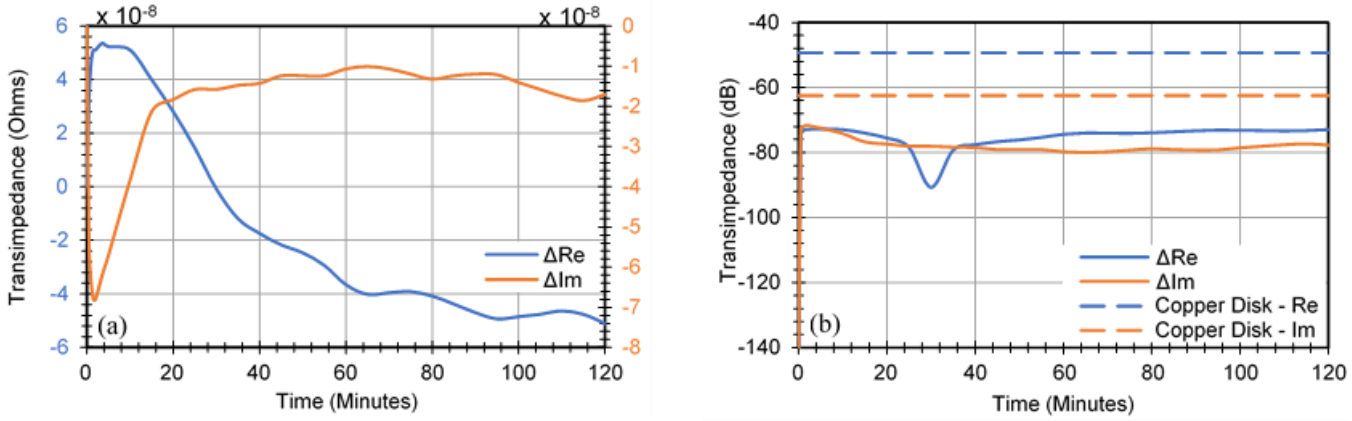

Fig. 8. Drift measurement data showing (a) the drift in measured real and imaginary transimpedance values plotted versus time and (b) absolutes of measured drift in real and imaginary transimpedance values in dB scale compared with the copper disk at 50 kHz.

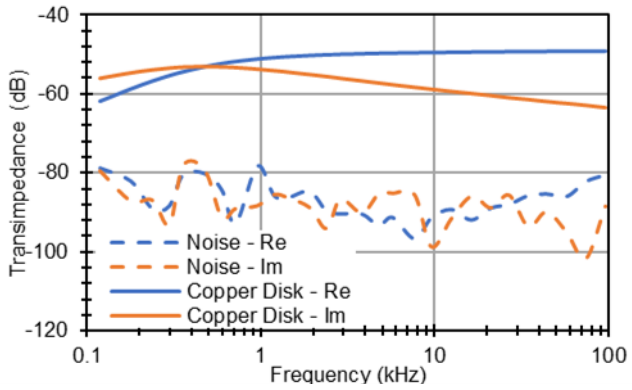

Fig. 9. Absolute of real and imaginary transimpedance values of example copper disk data compared with noise in dB scale.

IV. Method

An impedance analyser (*Solatron 1260A*) was used to measure the impedance characteristics of the coil arrangement. This was performed for the nine transmit coils connected in series wound in the same sense. This was also repeated for each receive coil. Impedance measurements were repeated five times to eliminate any error originating from noise contributions.

Before starting an experiment, all settings were set using the GUI and the system was left running for at least half an hour. This enabled the system to reach a steady-state temperature and minimize measurement drift caused by system temperature changes. Additionally, all experiments were performed in a temperature-controlled environment to prevent significant ambient temperature changes, in order to minimize thermal drift. A background measurement was first taken with no object in the coils. Then, this was subtracted from the measurements with the target object in the coils. After this, a NiZn ferrite rod (Ferroxcube ROD10/40-4B2-L) was placed in the coils for calibration as a pure real response is expected from the rod across the frequency range used. Phase correction for each frequency was done according to the ferrite rod's results using (9). The correction values were then restored and applied to all subsequent target measurements.

$$Z_{Calibrated} = Z_0 \times \frac{e^{-j\theta}}{|Z_0|} \tag{9}$$

The noise floor of the system was quantified by performing measurements with no object in the coils and then subtracting the background field from the measurements. Measurement drift was quantified by measuring transimpedance with no target object in the coils over a defined time scale and using the same background subtraction method for all measurements. Experimental repeatability was evaluated by repeating the same measurement protocol with a copper disk for ten times over a period of 48 hours. Each separate measurement lasted one hour and was temporally spaced by approximately two hours.

MPTs were acquired by rotating each target object in the coils twenty-four times with fifteen-degree steps using the target orientation manipulator in Fig. 4. After each rotational increment, the background field subtraction was updated to further minimize drift and improve experimental repeatability. After all orientations were measured, the control software calculated the MPTs and output MPT eigenvalues and the associated plots. A subset of target objects is shown in Fig. 5. The landmine surrogates were provided by Fenix Insight UK.

V. Coil Geometry Modeling and Simulations

The simulation geometry comprised of an outer free-space region and the coil arrangement simplified into segmented 3D rings of the nine transmit and eight receive coils as shown in Fig. 2(a). Coil excitation used current distributions normalized to the transmit coil with the fewest number of turns. Simulations for comparison with experimental measurements involved the rotation of the target object positioned in the most sensitive and uniform field region of the coil arrangement. Target rotations used 15° increments from 0° to 345° at either single fixed frequencies or spectroscopically in the range of 10 Hz to 100 MHz in ten logarithmic increments per decade. For disk targets typical meshing involved a FEM model of approximately 150k tetrahedral elements in total per rotational geometry with between 12k to 20k elements

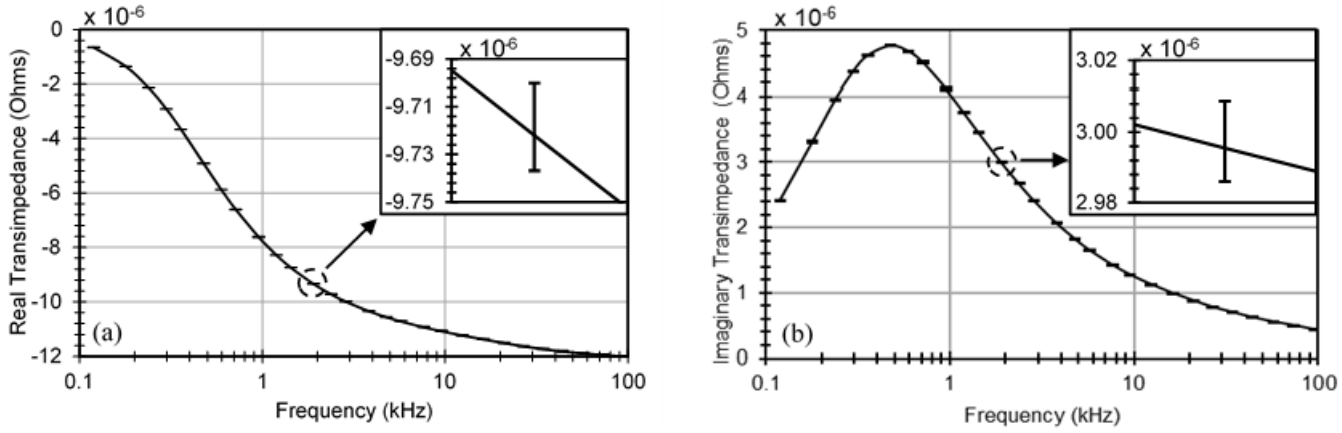

Fig. 10. Average of the transimpedance values of ten consecutive experiments with error bars showing the range of maximum and minimum values for each transimpedance. Plots show (a) real and (b) imaginary transimpedance values. The deviation in the data is approximately two orders of magnitude smaller compared with the absolute transimpedance values, which gives the appearance of single horizontal tick lines for the plotted error bars in the main plots. The upper right insert region in the plots shows the typical small deviation across the experiments, which is not easily discernible in the main plots. This is quantified in TABLE I.

per disk. This increasing to approaching 200k tetrahedral elements per whole FEM and approximately 30k elements for simulations involving cone targets. For the non-target case, 2D axial-symmetric- simulations were carried out to assess the field uniformity of the coil arrangement as shown in Fig. 6. The uniformity was verified by measuring the MPT of a stainless-steel ball bearing of 1 cm in diameter at various locations on and off-axis within the measurement region. The standard deviation of the MPT was found to be 30 mm^3, which is the same order of magnitude as the noise floor. Simulations were performed using the FEM solver, *Maxwell, (Ansys Electromagnetics Suite, Release 19.2)*.

VI. Coil Characterization and System Performance

Although both receive coils were designed to be identical, in practice, their impedances across the adopted frequency range were not the same. Coil Rx1 was found to exhibit a resonance peak at 371 kHz, while coil Rx2 yielded a resonance peak at approximately 478 kHz, due to differing lengths and spacing of constituent wires. To reduce the resonance effects, a parallel capacitance of 15 pF was used. Additionally, a parallel resistance of 43 kΩ was added to coil Rx1 and 56 kΩ was added to coil Rx2. The effect of the additional passive components on linearity and resonance is shown in Fig. 7(a). The addition of the passive component networks has effectively increased the linearity towards the higher end of the operating frequency spectrum. The measured transimpedance between the transmit and the receive coils are shown in Fig. 7(b). As seen from the plot, the resonance frequency is approximately 250 kHz, which is above the maximum operating frequency of the system.

System performance was measured by evaluating measurement drift, the noise floor characteristics and experimental repeatability. From the measured drift curves shown in Fig. 8(a), it can be clearly seen that most of the drift happens in the first sixty minutes. The results of the drift measurement were then compared to the transimpedance measurements of the copper disk at 50 kHz, shown as straight dashed lines, in Fig. 8(b). Time interval to update the background was determined by evaluating this figure. The measured noise floor was compared to transimpedance measurements of a copper disk having a diameter of 30 mm and thickness of 2 mm as shown in Fig. 9 in dB scale. As can be seen, there is a minimum of 20 dB difference between noise floor and signal across the measured frequency spectrum. In addition, the variance in MPT measurements is between −78 dB and −100 dB, which is approximately 15 mm^3.

Quantification of experimental repeatability was evaluated by using the largest and smallest values of the MPT eigenvalues for a given frequency in normalized RMS error (NRMSE) as defined by (10). In the NRMSE equation, n is number of measurement frequencies, $Expt_i$ is the maximum or minimum transimpedance value at frequency i, $Expt(Avg)_i$ is the average of the transimpedance values for frequency i and $\overline{Expt(Avg)}$ is the average of average transimpedance values for all frequencies. Lower NRMSE values mean better experimental repeatability.

$$\text{NRMSE} = \frac{\sqrt{\frac{\sum_{i=1}^{n} (\text{Expt}_i - \text{Expt(Avg)}_i)^2}{n}}}{\overline{\text{Expt(Avg)}}} \tag{10}$$

TABLE I presents the NRMSE values for the copper disk. Fig. 10 also shows the variation of eigenvalues from all experiments for each frequency compared to the average using error bars, where most of the maximum and minimum values can only be discerned as a single line. This represents a typical result of only 0.54% average difference between maximum and minimum real transimpedance values and 0.62% imaginary transimpedance values across all frequencies, which indicates excellent experimental repeatability.

VII. Results

MPTs of various objects were measured with the multi-coil arrangement and compared. A range of US Dollar coins were compared with simulations and measurements acquired from our previous measurement system, which were published in [32], [33]. Both simulations and previous measurements

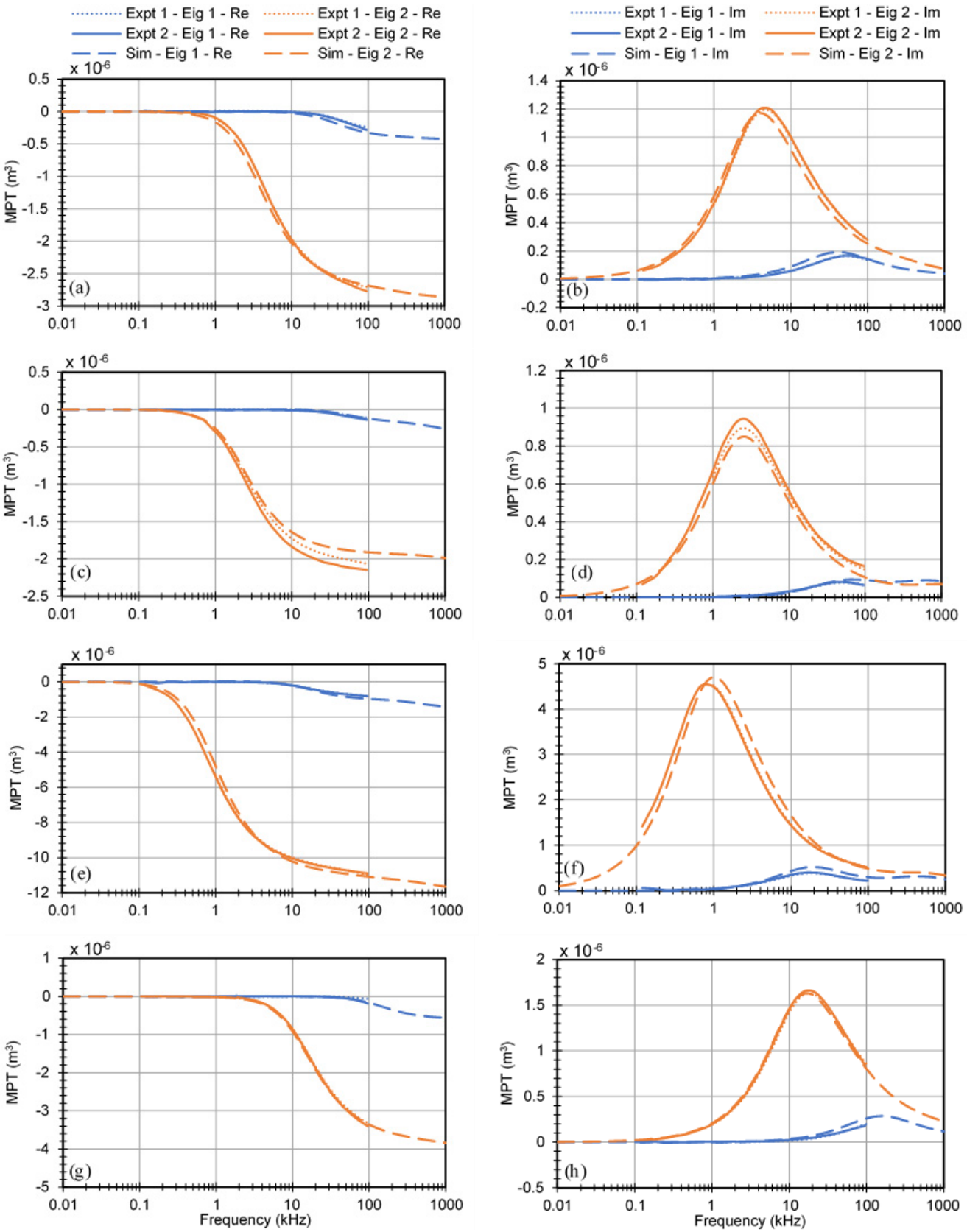

Fig. 11. Measured real and imaginary MPT eigenvalues for US coinage, compared with simulated and previously published MPT results are shown. Plots (a-b) one cent, (c-d) dime, (e-f) half dollar and (g-h) nickel. Expt 1 and Sim are values for experimental and simulated results from [33] while Expt 2 is experimental data from the new system.

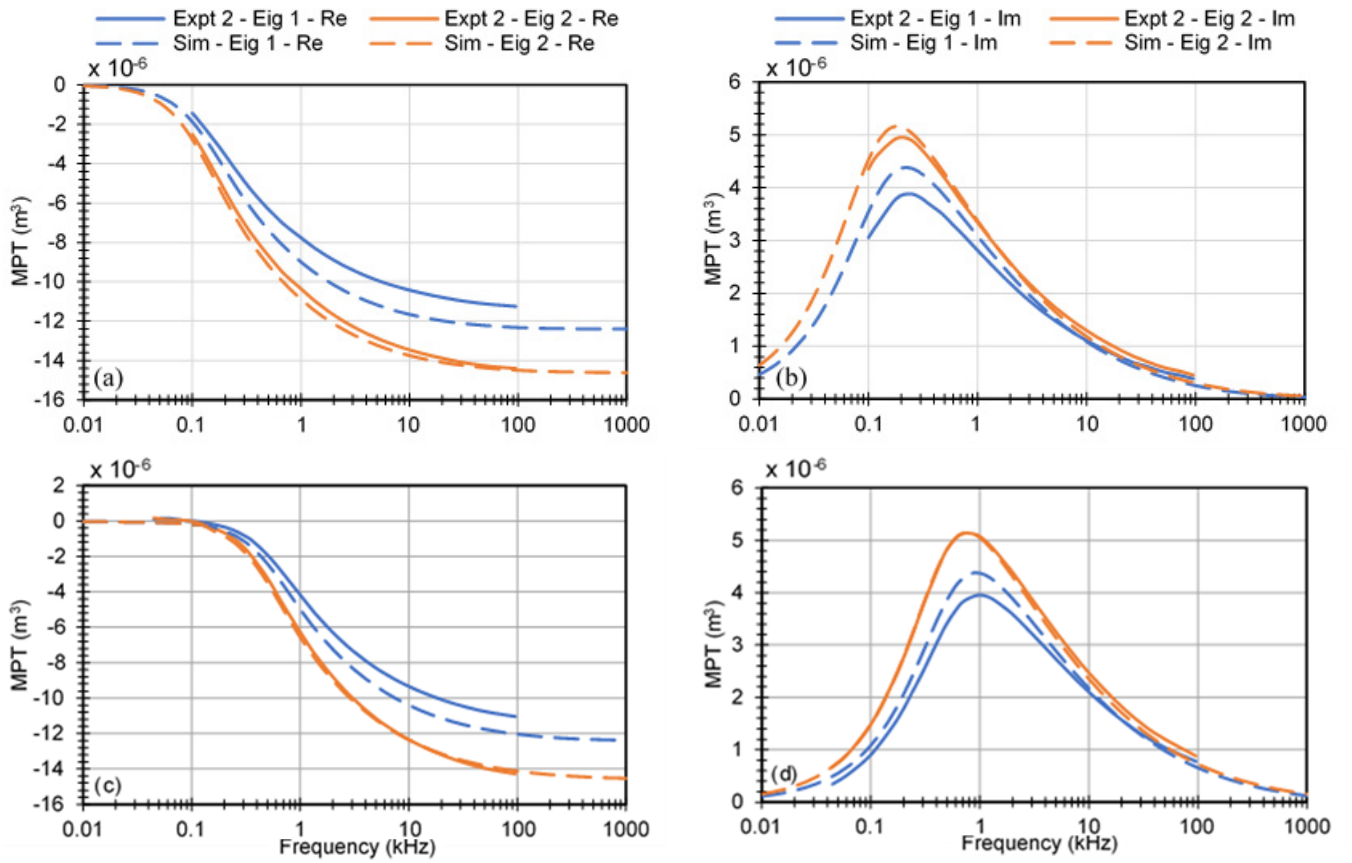

Fig. 12. Real and Imaginary MPT eigenvalues of two geometrically identical cones, which are 30 mm in both diameter and height. Plots (a-b) copper and (c-d) brass cones, respectively. Expt is experimental data from the new system and Sim is the simulated data. Conductivity of 58 MS/m and 13.9 MS/m were used for copper and brass cones, respectively.

TABLE I
NRMSE OF DIFFERENCES BETWEEN MAXIMUM AND MINIMUM TRANSIMPEDANCE EIGENVALUES COMPARED TO THE AVERAGE

	Real Eigenvalues		Imaginary Eigenvalues	
	Min	Max	Min	Max
Copper Disk	0.0017	0.0023	0.0033	0.0037

TABLE II
NRMSE OF DIFFERENCES BETWEEN MEASURED MPT EIGENVALUES COMPARED TO THE PREVIOUSLY PUBLISHED MEASURED AND SIMULATED MPT EIGENVALUES

	Experimental Eigenvalues				*Simulated Eigenvalues*			
	Eigenvalue 1		Eigenvalue 2		Eigenvalue 1		Eigenvalue 2	
	Re	Im	Re	Im	Re	Im	Re	Im
One Cent	0.270	0.052	0.023	0.025	0.516	0.300	0.073	0.091
Nickel	3.290	0.138	0.044	0.025	0.367	0.535	0.046	0.042
Dime	0.618	0.061	0.059	0.066	0.755	0.304	0.146	0.142
Half Dollar	0.072	0.043	0.009	0.021	0.273	0.305	0.042	0.108
Copper Cone	N/A	N/A	N/A	N/A	0.117	0.127	0.033	0.057
Brass Cone	N/A	N/A	N/A	N/A	0.125	0.095	0.033	0.039
Type 72A	0.370	0.032	0.597	0.048	N/A	N/A	N/A	N/A
TS-50	4.863	0.278	0.250	0.105	N/A	N/A	N/A	N/A

of objects' MPTs were used as a verification method of the system's ability to measure MPTs of objects, as MPTs are object specific and do not change depending on how they are obtained. Additionally, measured MPT's were compared with FEM simulations of copper and brass cones.

Fig. 11 shows objects measured, which are compared with both simulations and previous measurements, Fig. 12 shows objects measured, which are compared with simulations and Fig. 13 compares measured surrogate landmines with previous measurements. NRMSE values are shown for the experimental results in TABLE II compared with both previously published measured and simulated MPTs where available. NRMSE values comparing recent and past experimental data are shown in *Experimental Eigenvalues* column while the NRMSE values comparing recent experimental data with simulated data are shown in *Simulated Eigenvalues* column.

There is good agreement between experimental results for US coins with our previously published simulated and experimental data. For example, for the one-cent coin, recent experimental data acquired from the multi-coil arrangement, labelled Expt 2 follow the same curve with previously published experimental data, labelled Expt 1. Magnitudes and the horizontal positions of loss-peaks are within two percent for both eigenvalues. Loss-peak magnitudes for simulation and

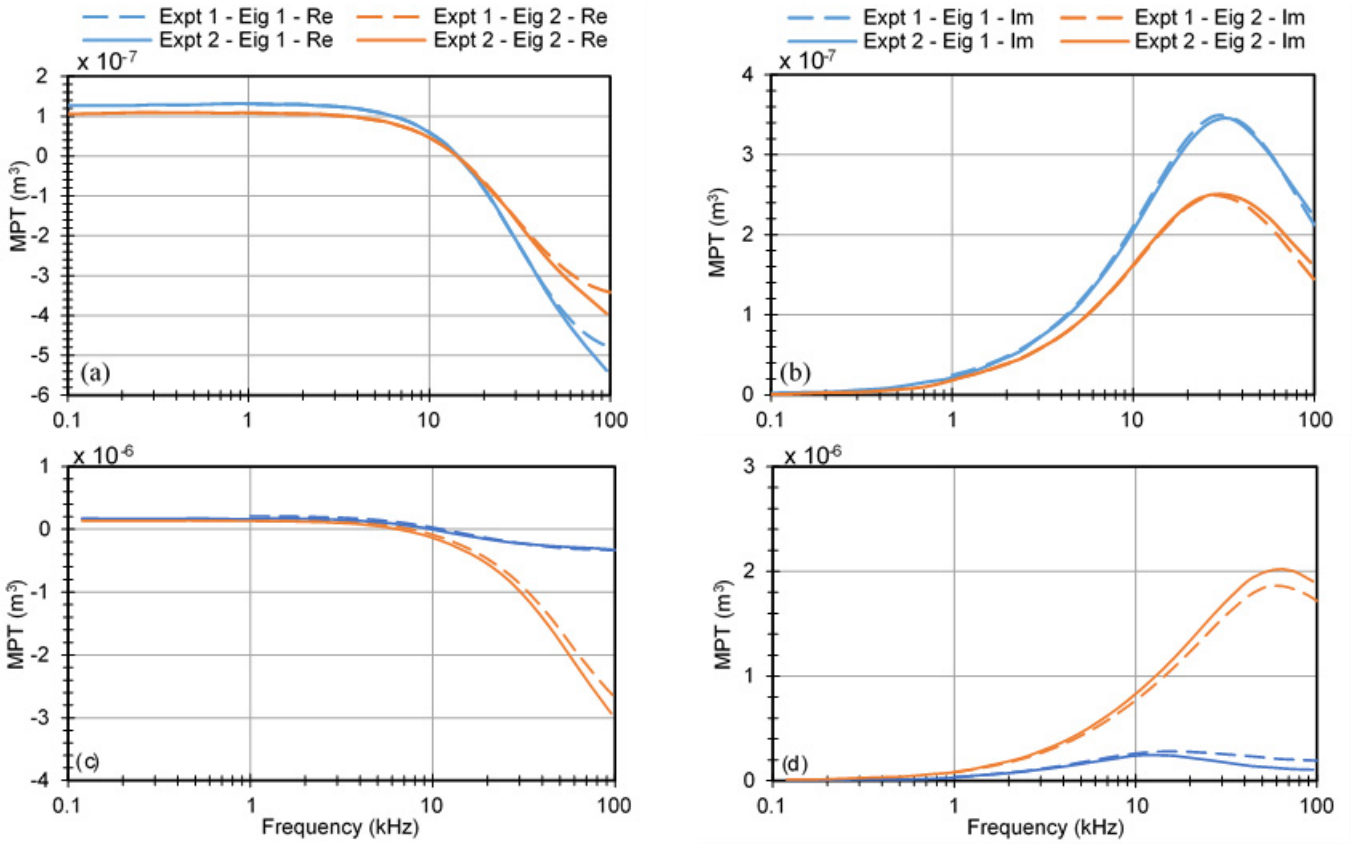

Fig. 13. Real and imaginary MPT eigenvalues of target anti-personnel landmines. Plot (a-b) Type-72A landmine surrogate and (c-d) TS-50 landmine surrogate. Expt 1 refers to previous experimental data from [32] and Expt 2 is for the experimental data from the new system.

experimental data are within twelve and three percent of each other for eigenvalue one and two, respectively.

Additionally, the magnitude of the measured MPT and frequency of the loss peak of the one cent coin are the same order of magnitude with the work of Scott and Larson [29]. However, a full comparison cannot be made as only five frequency points were presented in [29] while thirty are used in our system. Furthermore, [29] does not present full real and imaginary eigenvalue components which would allow for a direct comparison with our work.

The main source of error between experimental data collected with the new system and previous simulated data for US coins from [33] is due to simulation models assuming coins only to be simple cylinders with no attempt to describe additional geometrical features e.g. reeded edges, legend or design relief. Additionally, material composition of the coins was also assumed to be homogenous in simulations while this is not the case in physical reality, as coins are made of complex alloys. The inability of the FEM process to accurately describe the true physical and electrical nature of coins is more fully described in [33].

For cone shaped targets in Fig. 12 the overall agreement between experiment and simulation data are also generally good, with the FEM results validating the experimental data acquired from the coil arrangement. For example, for the copper cone, loss-peak magnitudes between experimental and simulated MPTs for eigenvalue 1 are within ten percent of each other and are within five percent for eigenvalue 2. Position of the loss-peaks in the frequency spectrum are within ten percent of each other for eigenvalue 1 and seven percent for eigenvalue 2. Such differences are to be expected due to the FEM model only being an approximate geometrical representation of the actual physical coil arrangement in terms of e.g. conductor thickness, coil positions and diameters. Additionally, for computational simplicity, the FEM model describes both transmit and receive coils as simplified segmented polygons. Similarly, to constrain the meshing level within the FEM, targets such as cones have been simplified using rounded edges, which are not present in physical reality. Simplifications of this type are a necessary trade-off between modelling accuracy and the available computational resources.

There is also a good agreement between measured surrogate landmine MPTs with previously published measured data. Magnitudes and the horizontal positions of the loss-peaks are within two percent of each other for the Type-72A surrogate landmine and within five percent for the TS-50 surrogate landmine. There is an upward trend towards the end of the spectrum of real MPT eigenvalues measured by the previous system for Type-72A surrogate landmine. This is potentially caused by the generated magnetic field not being entirely uniform in the previous system for the volume covered by the landmine. In addition, the higher NRMSE values for real MPT eigenvalues for both landmines are caused by the MPT curves changing signs through the frequency spectrum.

VIII. Conclusion and Future Work

A multi-coil arrangement system has been designed and constructed for accurately measuring MPTs of anti-personnel (AP) landmines and similar sized metallic objects. Noise and drift performance of the system in addition to experimental repeatability have been presented. Experimental results were compared with previously published simulated and experimental data, which proved the ability of the system for measuring MPTs of objects. This verified the ability of the system to measure MPTs accurately. The novelty of the presented coil arrangement is its ability to generate a primary field of sufficient uniformity to satisfy the rank-2 MPT dipole approximation described by (2) for three-dimensional target interrogation of large objects such as AP landmines.

Measuring MPTs of non-symmetrical objects by improving software and building a target orientation manipulator that can automatically rotate objects in three-dimensional space are the main areas of future work. This will then allow the building of a comprehensive MPT library containing anti-personnel landmines and common metallic clutter found in post-conflict areas. The future challenge will be to apply such a library initially to aid in the development of efficient metal detection algorithms and subsequently, to provide a real-time comparison within the field with metal detection technology capable of providing direct MPT measurements. However, to utilize the MPT in practical demining operations several challenges need to be addressed to discriminate between clutter items and AP landmines. In particular, multiple lateral sensor spacing needs to exist to correctly interrogate the target in three-dimensional space for MPT inversion. Additionally, highly magnetic soils pose a challenge for accurate MPT measurement due to the electromagnetic behaviour of soils [44]. The issues of lateral and multiple coil spacing has been described in [10], [12] and is the topic of ongoing research in [19]. Once these issues are further understood, laboratory-based instruments for accurately measuring MPTs such as the one presented in this paper, will be vital in aiding the reduction of false alarms in the field.

References

[1] *What Is a Landmine?* Int. Campaign Ban Landmines, Geneva, Switzerland, 2019.

[2] *Facts About Landmines*, CARE, Noida, India, 2019.

[3] *Landmine Monitor*, Int. Campaign Ban Landmines, Geneva, Switzerland, 2019.

[4] *The Landmine History Page*, Fed. Amer. Scientists, Washington, DC, USA, 2019. [Online]. Available: https://fas.org/asmp/campaigns/landmines/lmhistory.htm

[5] K. Tsipis, "Technological innovation in humanitarian demining," in *Proc. Hum. Factors Ergonom. Soc.*, Santa Monica, CA, USA, 1998, pp. 750–753.

[6] P. D. Ledger and W. R. B. Lionheart, "Understanding the magnetic polarizability tensor," *IEEE Trans. Magn.*, vol. 52, no. 5, pp. 1–16, May 2016.

[7] P. D. Ledger and W. R. B. Lionheart, "An explicit formula for the magnetic polarizability tensor for object characterization," *IEEE Trans. Geosci. Remote Sens.*, vol. 56, no. 6, pp. 3520–3533, Jun. 2018.

[8] P. D. Ledger and W. R. B. Lionheart, "The spectral properties of the magnetic polarizability tensor for metallic object characterisation," *Math. Methods Appl. Sci.*, vol. 43, no. 1, pp. 78–113, Jan. 2020.

[9] P. D. Ledger and W. R. B. Lionheart, "Generalised magnetic polarizability tensors," *Math. Methods Appl. Sci.*, vol. 41, no. 8, pp. 3175–3196, May 2018.

[10] J. P. Fernandez, B. E. Barrowes, T. M. Grzegorczyk, N. Lhomme, K. O'Neill, and F. Shubitidze, "A man-portable vector sensor for identification of unexploded ordnance," *IEEE Sensors J.*, vol. 11, no. 10, pp. 2542–2555, Oct. 2011.

[11] S. J. Norton and I. J. Won, "Identification of buried unexploded ordnance from broadband electromagnetic induction data," *IEEE Trans. Geosci. Remote Sens.*, vol. 39, no. 10, pp. 2253–2261, Oct. 2001.

[12] T. M. Grzegorczyk, B. E. Barrowes, F. Shubitidze, J. P. Fernandez, and K. O'Neill, "Simultaneous identification of multiple unexploded ordnance using electromagnetic induction sensors," *IEEE Trans. Geosci. Remote Sens.*, vol. 49, no. 7, pp. 2507–2517, Jul. 2011.

[13] J. Makkonen *et al.*, "KNN classification of metallic targets using the magnetic polarizability tensor," *Meas. Sci. Technol.*, vol. 25, no. 5, May 2014, Art. no. 055105.

[14] M. D. O'Toole, N. Karimian, and A. J. Peyton, "Classification of nonferrous metals using magnetic induction spectroscopy," *IEEE Trans. Ind. Informat.*, vol. 14, no. 8, pp. 3477–3485, Aug. 2018.

[15] Y. Tao, W. Yin, W. Zhang, Y. Zhao, C. Ktistis, and A. J. Peyton, "A very-low-frequency electromagnetic inductive sensor system for workpiece recognition using the magnetic polarizability tensor," *IEEE Sensors J.*, vol. 17, no. 9, pp. 2703–2712, May 2017.

[16] J. García-Martín, J. Gómez-Gil, and E. Vázquez-Sánchez, "Non-destructive techniques based on eddy current testing," *Sensors*, vol. 11, no. 3, pp. 2525–2565, Feb. 2011.

[17] L. U. Daura, G. Tian, Q. Yi, and A. Sophian, "Wireless power transfer-based eddy current non-destructive testing using a flexible printed coil array," *Phil. Trans. Roy. Soc. A, Math., Phys. Eng. Sci.*, vol. 378, no. 2182, Oct. 2020, Art. no. 20190579.

[18] M. Lu *et al.*, "Determination of surface crack orientation based on thin-skin regime using triple-coil drive–pickup eddy-current sensor," *IEEE Trans. Instrum. Meas.*, vol. 70, Dec. 2021, Art. no. 6003509.

[19] D. Ambrus, D. Vasic, and V. Bilas, "Comparative study of planar coil EMI sensors for inversion-based detection of buried objects," *IEEE Sensors J.*, vol. 20, no. 2, pp. 968–979, Jan. 2020.

[20] Y. Zhao, W. Yin, C. Ktistis, D. Butterworth, and A. J. Peyton, "Determining the electromagnetic polarizability tensors of metal objects during in-line scanning," *IEEE Trans. Instrum. Meas.*, vol. 65, no. 5, pp. 1172–1181, May 2016.

[21] B. Dekdouk, C. Ktistis, L. A. Marsh, D. W. Armitage, and A. J. Peyton, "Towards metal detection and identification for humanitarian demining using magnetic polarizability tensor spectroscopy," *Meas. Sci. Technol.*, vol. 26, no. 11, Nov. 2015, Art. no. 115501.

[22] D. Ambrus, D. Vasic, and V. Bilas, "Innovating on top of I&M fundamentals for safer humanitarian demining," *IEEE Instrum. Meas. Mag.*, vol. 23, no. 3, pp. 35–41, May 2020.

[23] Y. Dalichaouch *et al.*, "Wideband frequency response of low-metal mines," *Proc. SPIE, Detection Remediation Technol. Mines Minelike Targets IX*, vol. 5415, Sep. 2004, doi: 10.1117/12.547340.

[24] W. R. Scott and G. D. Lars, "Modeling the measured em induction response of targets as a sum of dipole terms each with a discrete relaxation frequency," in *Proc. IEEE Int. Geosci. Remote Sens. Symp.*, Honolulu, HI, USA, Jul. 2010, pp. 4188–4191.

[25] G. D. Larson and W. R. Scott, Jr., "Automated, non-metallic measurement facility for testing and development of electromagnetic induction sensors for landmine detection," *Proc. SPIE, Detection Sens. Mines, Explosive Objects, Obscured Targets XIV*, vol. 7303, May 2009, Art. no. 73030X, doi: 10.1117/12.819855.

[26] R. B. Goldfarb and J. V. Minervini, "Calibration of AC susceptometer for cylindrical specimens," *Rev. Sci. Instrum.*, vol. 55, no. 5, pp. 761–764, May 1984.

[27] G. F. West and R. C. Bailey, "An instrument for measuring complex magnetic susceptibility of soils," *Proc. SPIE, Detection Remediation Technol. Mines Minelike Targets X*, vol. 5794, Jun. 2005, doi: 10.1117/12.602992.

[28] W. R. Scott, "Broadband array of electromagnetic induction sensors for detecting buried landmines," in *Proc. IEEE Int. Geosci. Remote Sens. Symp. (IGARSS)*, Boston, MA, USA, Jul. 2008, pp. II-375–II-378.

[29] W. R. Scott and G. D. Larson, "Measured dipole expansion of discrete relaxations to represent the electromagnetic induction response of buried metal targets," in *Detection and Sensing of Mines, Explosive Objects, and Obscured Targets XV*, 2010, Art. no. 76640E.

[30] W. R. Scott and M. McFadden, "Wideband measurement of the magnetic susceptibility of soils and the magnetic polarizability of metallic objects," in *Proc. IEEE Int. Geosci. Remote Sens. Symp.*, Munich, Germany, Jul. 2012, pp. 3170–3173.

[31] O. A. Abdel Rehim, J. L. Davidson, L. A. Marsh, M. D. O'Toole, D. W. Armitage, and A. J. Peyton, "Measurement system for determining the magnetic polarizability tensor of small metal targets," in *Proc. IEEE Sensors Appl. Symp. (SAS)*, Zadar, Croatia, Apr. 2015, pp. 1–5.

[32] O. A. Abdel-Rehim, J. L. Davidson, L. A. Marsh, M. D. O'Toole, and A. J. Peyton, "Magnetic polarizability tensor spectroscopy for low metal anti-personnel mine surrogates," *IEEE Sensors J.*, vol. 16, no. 10, pp. 3775–3783, May 2016.
[33] J. L. Davidson, O. A. Abdel-Rehim, P. Hu, L. A. Marsh, M. D. O'Toole, and A. J. Peyton, "On the magnetic polarizability tensor of US coinage," *Meas. Sci. Technol.*, vol. 29, no. 3, Mar. 2018, Art. no. 035501.
[34] P. D. Ledger and W. R. B. Lionheart, "Characterizing the shape and material properties of hidden targets from magnetic induction data," *IMA J. Appl. Math.*, vol. 80, no. 6, pp. 1776–1798, 2015.
[35] L. A. Marsh, C. Ktistis, A. Järvi, D. W. Armitage, and A. J. Peyton, "Three-dimensional object location and inversion of the magnetic polarizability tensor at a single frequency using a walk-through metal detector," *Meas. Sci. Technol.*, vol. 24, no. 4, Apr. 2013, Art. no. 045102.
[36] L. A. Marsh, C. Ktistis, A. Järvi, D. W. Armitage, and A. J. Peyton, "Determination of the magnetic polarizability tensor and three dimensional object location for multiple objects using a walk-through metal detector," *Meas. Sci. Technol.*, vol. 25, no. 5, May 2014, Art. no. 055107.
[37] B. Dekdouk, L. A. Marsh, D. W. Armitage, and A. J. Peyton, "Estimating magnetic polarizability tensor of buried metallic targets for land mine clearance," in *Ultra-Wideband, Short-Pulse Electromagnetics 10*, F. Sabath and E. Mokole, Eds. New York, NY, USA: Springer, 2014, doi: 10.1007/978-1-4614-9500-0_38.
[38] A. Bjorck, *Numerical Methods in Matrix Computations*. Cham, Switzerland: Springer, 2016. [Online]. Available: https://www.springer.com/gp/book/9783319050881
[39] T. H. Bell, B. J. Barrow, and J. T. Miller, "Subsurface discrimination using electromagnetic induction sensors," *IEEE Trans. Geosci. Remote Sens.*, vol. 39, no. 6, pp. 1286–1293, Jun. 2001.
[40] GICHD. *Collaborative ORDnance Data Repository (CORD)*. Accessed: Apr. 10, 2021. [Online]. Available: http://cord.gichd.org/ordnance?id=http%3A%2F%2Fcord.gichd.org%2Fontology%23Landmine4156
[41] E. L. Bronaugh, "Helmholtz coils for calibration of probes and sensors: Limits of magnetic field accuracy and uniformity," in *Proc. Int. Symp. Electromagn. Compat.*, Atlanta, GA, USA, 1995, pp. 72–76.
[42] L. A. Marsh *et al.*, "Combining electromagnetic spectroscopy and ground-penetrating radar for the detection of anti-personnel landmines," *Sensors*, vol. 19, no. 15, p. 3390, Aug. 2019.
[43] W. van Verre, L. A. Marsh, J. L. Davidson, E. Cheadle, F. J. W. Podd, and A. J. Peyton, "Detection of metallic objects in mineralized soil using magnetic induction spectroscopy," *IEEE Trans. Geosci. Remote Sens.*, vol. 59, no. 1, pp. 27–36, Jan. 2021.
[44] Y. Das, "Effects of soil electromagnetic properties on metal detectors," *IEEE Trans. Geosci. Remote Sens.*, vol. 44, no. 6, pp. 1444–1453, Jun. 2006.

Toykan Özdeğer received the M.Eng. (Hons.) degree in electrical and electronics engineering from The University of Manchester in 2018, where he is currently pursuing the Ph.D. degree. From 2016 to 2017, he worked as an Instrumentation and Control Engineering Placement Student with Phillips 66 for one year during his degree. His research interests include machine learning, landmine detection, and metal characterization.

John L. Davidson received the B.Sc. (Hons.) degree in engineering physics and the Ph.D. degree in mössbauer spectroscopy from Sheffield Hallam University (SHU) in 1993 and 1997, respectively. As a Research Fellow with the University of Southampton from 1998 to 2002, he developed an interest in electrostatics and electromagnetics. In 2002, he joined The University of Manchester initially working in the area of electrical impedance tomography applied to industrial and medical problems, and more recently, in the area of electromagnetics. He has authored or coauthored more than 50 scientific publications. His current research interests include electromagnetic modeling, inverse problems, and magnetic induction sensor development. In 2008, he was awarded the Beloe Fellowship Award from Worshipful Company of Scientific Instrument Makers.

Wouter van Verre received the B.Eng. (Hons.) degree in electrical and electronics engineering and the Ph.D. degree in the use of electromagnetic methods for the detection of buried landmines from The University of Manchester in 2016 and 2021, respectively. He subsequently joined the EM Sensing Group, Department of Electrical and Electronic Engineering, The University of Manchester. His research interests include the use of metal detection in polar environments and MIMO ground-penetrating radar.

Liam A. Marsh (Member, IEEE) received the M.Eng. (Hons.) degree in electrical engineering and electronics from the Institute of Science and Technology, The University of Manchester, Manchester, U.K., in 2007, and the Ph.D. degree in electromagnetic tomography and people screening from The University of Manchester in 2011. He subsequently joined the Sensing, Imaging and Signal Processing Research Group, Department of Electrical and Electronic Engineering, The University of Manchester, as a Research Associate. In 2018, he was appointed as a Lecturer in Embedded Systems with The University of Manchester. His research interests include the development of electromagnetic sensor systems for security, landmine detection, and polar sensing.

William R. B. Lionheart received the B.Sc. degree in mathematics from The University of Warwick, U.K., in 1980, and the Ph.D. degree in electrical impedance tomography from Oxford Brookes University, U.K.

He is currently a Professor of Applied Mathematics with The University of Manchester, U.K., where he is involved in a wide range of inverse problems in medicine and industry, including electrical impedance tomography, magnetic induction tomography, x-ray and neutron computed tomography, and position emission tomography. His interest in low-frequency electromagnetic imaging led to his involvement in civilian land mine clearance.

Anthony J. Peyton received the B.Sc. degree in electrical engineering and electronics from The University of Manchester in 1983 and the Ph.D. degree in medical instrumentation in 1986. After various positions in the scientific instrumentation industry and academia, he was appointed as a Professor in Electromagnetic Engineering in May 2004. He has over 30 years of experience in a diverse range of electromagnetic sensor systems and has been a principal investigator of numerous national, international and industry funded projects. He has been the coauthor of over 160 international journal articles. His group work was extensively with industry in sectors, including non-destructive testing, security, medical, food quality, and humanitarian demining.